Rashba splitting in bilayer transition metal dichalcogenides controlled by electronic ferroelectricity

Zuzhang Lin,[1,2] Chen Si [ORCID],[3,*] Shaorong Duan,[2] Chong Wang [ORCID],[1,2] and Wenhui Duan [ORCID][1,2,4]

[1]*Institute for Advanced Study, Tsinghua University, Beijing 100084, China*
[2]*State Key Laboratory of Low Dimensional Quantum Physics and Department of Physics, Tsinghua University, Beijing, 100084, China*
[3]*School of Materials Science and Engineering, Beihang University, Beijing 100191, China*
[4]*Collaborative Innovation Center of Quantum Matter, Tsinghua University, Beijing 100084, China*

Based on first-principles calculations and $\boldsymbol{k} \cdot \boldsymbol{p}$ model analyses, we uncover the coexistence and coupling of Rashba spin splitting with electronic ferroelectricity in bilayer transition metal dichalcogenides MX_2 ($M =$ Mo,W; $X =$ S,Se,Te) with certain stacking configurations. The reversible spontaneous ferroelectric polarization, along the out-of-plane direction (the preferred direction for applications), totally arises from the interlayer charge transfer, rather than being governed by the ionic displacement as found in conventional ferroelectrics. The spin texture related to the Rashba spin splitting can be reversed upon inversion of the ferroelectric polarization. In particular, by applying a small in-plane compressive strain, the magnitude of Rashba band splitting can be tuned to be as large as 100 meV. These results would open up possibilities for exploring two-dimensional multiferroic physics and developing electrically controlled nanoscale spintronic devices.

I. INTRODUCTION

Ferroelectric Rashba semiconductors (FRSCs) are a new class of multifunctional materials in which the ferroelectric polarization straightforwardly couples to the spin texture related to the Rashba spin splitting, thereby enabling control over the spin via electric control of the polarization [1]. Such a unique feature sets FRSCs apart from conventional magnetic semiconductors that still suffer from the requirements of external magnetic fields and low-temperature operations to control spin [2]. Therefore, FRSCs are highly promising for applications in spintronics [3], allowing us to design novel devices with nonvolatile logical functions. α-GeTe was the first FRSC predicted [4], and its spin texture has been experimentally confirmed to be reversed when the ferroelectric polarization is switched [5,6]. Subsequently, a handful of bulk materials including $BiAlO_3$ [7], LiZnSb [8], Bi_2WO_6 [9], and three halide perovskites [10] were also theoretically proposed to be FRSCs. Meanwhile, driven by the technological demands for miniaturization of devices in recent years, rapidly increasing attention has been paid to ultrathin two-dimensional (2D) materials. In this context, searching for or designing 2D FRSCs would be more appealing for nanoscale electronics and spintronics.

A good 2D FRSC is expected to satisfy the following conditions: (i) It should have reversible spontaneous polarization, particularly in the out-of-plane direction, the preferred direction for applications [11,12]. However, the vertical ferroelectricity usually vanishes as the film thickness becomes smaller than a critical value, due to the strengthened de-

polarization field and the reduced electronic screening [13]. So far, very few 2D materials are predicted to possess out-of-plane ferroelectricity [14,15], and among them only the ferroelectricity of In_2Se_3 has been verified experimentally [16,17], to the best of our knowledge. (ii) It should have a strong spin-orbit coupling (SOC) generating a large Rashba spin splitting [18–22]. Moreover, the energy barrier for reversing the ferroelectric polarization could not be too large, so as to ensure that spin texture can be easily manipulated [23,24]. (iii) It should be structurally stable and easily fabricated. Recently, although the coexistence of ferroelectricity and Rashba splitting was predicted in d1T-type monolayer transition metal dichalcogenides (TMDs) MX_2 ($M =$ Mo,W; $X =$ S,Se,Te) [25] and group IV binary monolayers SiGe, SiSn, GeSn, etc. [26], the former are not thermally stable compared to their 2H phase except WTe_2, and the latter are hypothetical materials, having not been synthesized. Additionally, the Rashba splitting in these two classes of materials is almost negligible, which hinders their practical spintronic applications.

In this paper, using first-principles calculations, we predict a class of promising 2D FRSCs in bilayer 2H-MX_2. Whereas the out-of-plane polarization is forbidden in monolayer 2H-MX_2 due to the presence of mirror symmetry, the bilayer 2H-MX_2 formed by stacking two monolayers in certain ways can exhibit out-of-plane ferroelectricity that arises totally from the interface dipole induced by the interlayer charge transfer. Two sets of Rashba splitting are observed in the highest four valence bands, with corresponding spin textures reversible by switching the ferroelectric polarization. More interestingly, we find that by applying a small in-plane compressive biaxial strain, the magnitude of the Rashba band splitting can be increased to more than 100 meV, i.e., a giant Rashba splitting
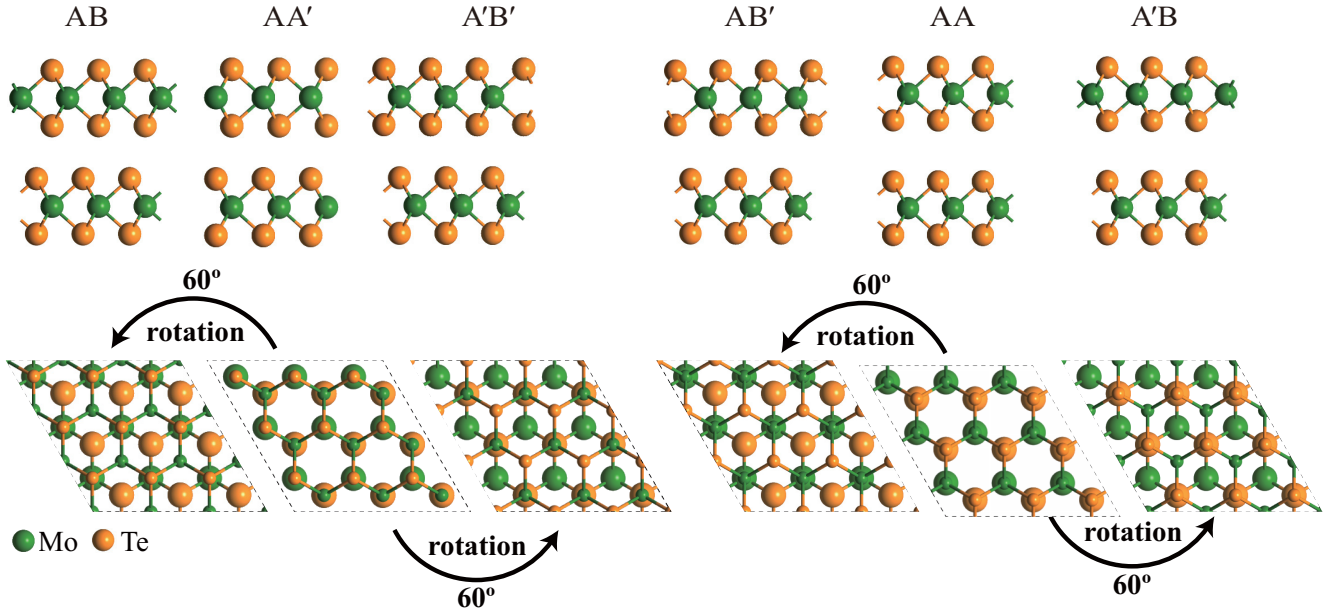
*sichen@buaa.edu.cn

FIG. 1. Side (upper panel) and top (lower panel) views of six high-symmetry stacking configurations of bilayer MoTe$_2$ (AB, AA', $A'B'$, AB', AA, and $A'B$). Green and orange balls represent Mo and Te atoms, respectively. AB (AB') and $A'B'$ ($A'B$) can be obtained via 60° clockwise and anticlockwise rotation of the top layer in the AA' (AA) configuration, respectively. In the lower panels, big spheres and small spheres are used to represent atoms in the bottom and top layers, respectively.

is achieved. We also develop a $k \cdot p$ model that explains well the physical origin of the Rashba splitting and its coupling with ferroelectricity.

II. METHODS

Our calculations are performed by using density functional theory (DFT), which is implemented in the Vienna ab initio simulation package [27,28]. To describe the ion-electron interaction, the projector-augmented wave potentials are used [29]. We adopt the generalized gradient approximation of Perdew-Burke-Ernzerhof [30,31] for the exchange-correlation functional and an energy cutoff of 400 eV for the plane-wave basis expansion. The van der Waals interaction is included by the dispersion-corrected DFT method (DFT-D3) [32]. The vacuum separation between periodic slabs is set to be more than 15 Å. The dipole corrections are added to cancel the errors of the electrostatic potential, atomic forces, and total energies under the periodic boundary condition. All the structures are optimized until the residual force on each atom is smaller than 0.001 eV Å^{-1}. In the self-consistent electronic calculation, SOC is included and the stopping criterion for energy convergence is 10^{-7} eV. A $16 \times 16 \times 1$ k-point mesh is used uniformly over the Brillouin zone. The climbing image nudged elastic method (CI-NEB) [33] is used to determine the energy barrier of the ferroelectric phase transition. The ferroelectric polarization is computed by the Berry phase method [34].

III. RESULTS AND DISCUSSION

A. Out-of-plane ferroelectricity

When two monolayer 2H-MX_2 are stacked into a bilayer, the weak van der Waals forces, responsible for cohesion,

allow the mutual sliding or rotation of adjacent layers, leading to different stacking orders. Here, we consider six possible high-symmetry stacking orders and name them according to the nomenclature in previous works [35–37], as shown in Fig. 1. Specifically speaking, AA' belongs to the point group D_{3d}, corresponding to the stacking in the 2H phase of bulk MX_2. AA belongs to the point group D_{3h} and can be gotten by exchanging the sites of M and X atoms in the top layer of AA'. The AB (AB') and $A'B'$ ($A'B$) stackings can be obtained via 60° clockwise and anticlockwise rotation of the top layer in the AA' (AA) stacking, respectively (see Fig. 1).

In the six high-symmetry stacking configurations of bilayer MX_2, the AA' is the most stable and possesses the lowest total energy [35], followed by two energetically degenerate configurations AB and $A'B'$, which have the second lowest energy (see Table I). However, the energy difference between AA' and AB ($A'B'$) is quite small, in the range of 0–13 meV per unit cell, in particular only 0.6 meV for bilayer MoS$_2$ (see Table II), indicating the ease of formations of AB and $A'B'$.

TABLE I. Lattice constants a, interlayer distances d, total energies E, and electronic polarizations P for bilayer MoTe$_2$ with different stacking configurations. The total energy of the most stable configuration is set as the reference of zero energy.

Stacking order	a (Å)	d (Å)	E (meV)	P (e/cm^2)
AB	3.520	3.46	13	-5.76×10^{11}
$A'B'$	3.520	3.46	13	5.76×10^{11}
AB'	3.520	3.63	41	0
$A'B$	3.516	4.10	105	0
AA'	3.517	3.41	0	0
AA	3.516	4.14	109	0

TABLE II. Total energy ΔE relative to the most stable stacking configuration AA', electronic polarization P, and Rashba coefficients λ_1 and λ_2 for the two sets of Rashba splitting of bilayer MX_2 with the ferroelectric AB configuration. λ_1 and λ_2 for MoS_2 and WS_2 are not given (NG) because of their small values beyond the DFT computational accuracy.

Systems	ΔE (meV)	P (e/cm^2)	λ_1 (eV Å)	λ_2 (eV Å)
$MoTe_2$	13	-5.76×10^{11}	0.026	0.058
MoS_2	0.6	-9.73×10^{11}	NG	NG
$MoSe_2$	3	-7.87×10^{11}	0.019	0.016
WS_2	12.7	-8.80×10^{11}	NG	NG
WSe_2	6	-8.38×10^{11}	0.017	0.022
WTe_2	18	-6.64×10^{11}	0.027	0.053

In fact, the AB stacking order has appeared in the natural bulk $3R$ phase of MX_2 [38,39]. Experimentally, the bilayer AA' and AB configurations have been synthesized by tuning the growth temperature in the chemical vapor deposition [40,41]. Other stacking orders could be evolved from the AA' or AB through interlayer shear displacement, which could be experimentally realized by interface friction [42]. Additionally, the bilayer TMD with different stacking orders can also be prepared by mechanically stacking two crystalline monolayers with different twisted angles [43].

Next, using bilayer $MoTe_2$ as an example, we show the presence of out-of-plane ferroelectricity in the AB and $A'B'$ configurations of bilayer MX_2. Table I summarizes the electronic polarizations of bilayer $MoTe_2$ in different stacking orders calculated by the Berry phase approach. It is found that AB and $A'B'$ show spontaneous polarizations with the same magnitude (5.76×10^{11} e/cm^2) but opposite polarizing directions ($-z$ and $+z$, z is perpendicular to the surface of bilayer MX_2). By contrast, the other four stacking configurations possess no polarizations. Using the CI-NEB method, we further calculate the transition pathway connecting AB and $A'B'$, which yields a barrier for reversing the electronic polarization of only 19.6 meV [see Fig. 2(a)]. This barrier is close to the transition barrier of the popular ferroelectric $BaTiO_3$ (11.2 meV calculated by PBE [44]), suggesting the feasibility of a ferroelectric switch in bilayer $MoTe_2$ under ambient conditions.

The emergence of vertical ferroelectricity in AB and $A'B'$ configurations of bilayer $MoTe_2$ arises from the breaking of both inversion and mirror symmetries as well as the net interlayer charge transfer. In monolayer $MoTe_2$, the presence of the m_z mirror symmetry (the m_z operator is defined as $m_z : z \rightarrow -z$) excludes any possible polarization along the z direction. When two $MoTe_2$ single layers are stacked in the AB or $A'B'$ order, the formed asymmetric bilayer structure possesses neither inversion symmetry nor m_z symmetry, allowing a net charge transfer between the top and bottom layers, which further creates an interface dipole accompanied by a potential step ΔV formed across the interface [45]. Figures 2(b)–2(d) show the plane-averaged electrostatic potential of bilayer $MoTe_2$ in different stacking orders along the z direction. In the AA', AA, AB', and $A'B$ configurations with inversion symmetry or mirror symmetry, there is no potential
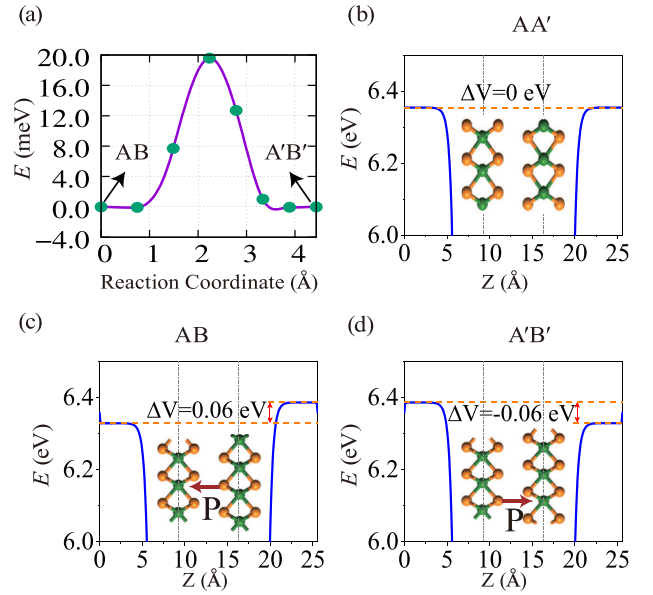

FIG. 2. (a) Total energy change of bilayer $MoTe_2$ during the structural phase transition from AB to $A'B'$ inducing the inversion of ferroelectric polarization. (b)–(d) Plane averaged electrostatic potentials of bilayer $MoTe_2$ in AA', AB, and $A'B'$ stacking configurations along the z directions.

step ΔV (for clarity, only the data for the AA' are shown). However, in the ferroelectric AB and $A'B'$ configurations, we observe a discontinuity of 0.06 eV between the vacuum levels on the top and bottom layers, corresponding to $\Delta V = 0.06$ eV for AB and $\Delta V = -0.06$ eV for $A'B'$, respectively. The sign of ΔV is determined by the orientation of the net charge transfer. Here, a net charge transfer from the bottom (top) layer to the top (bottom) layer leads to an interface dipole with the orientation along the $-z$ ($+z$) direction and a positive (negative) ΔV. Evidently, the opposite signs of ΔV in AB and $A'B'$ configurations exactly correspond to opposite polarization directions. On the other hand, the magnitude of ΔV is related to the interface dipole density: $\Delta V = 4\pi n$, where n is the interface dipole density of the slab [46]. This indicates that the larger the ΔV is, the larger is the interface dipole and the resultant ferroelectric polarization.

Similar to the case of bilayer $MoTe_2$, the structures AB and $A'B'$ of the other four bilayers MX_2 (MoS_2, $MoSe_2$, WS_2, and WSe_2) also show out-of-plane ferroelectricity with opposite electronic polarizations. The magnitudes of their polarizations are all of the order of 10^{11} e/cm^2 (see Table II), suggesting comparable interlayer charge transfer amounts in these bilayer TMD systems.

Additionally, the difference in the ferroelectric mechanism between the bilayer MX_2 and the traditional ferroelectrics such as $BaTiO_3$ [47] is worth mentioning. It is well known that the polarization in periodic systems can be divided into ionic polarization and electronic polarization [48], arising from asymmetric distribution of charged ions and the displacement of the electronic wave functions [34,49,50], respectively. The ferroelectricity in conventional ferroelectrics is usually dominated by ionic polarization accompanied by small electronic
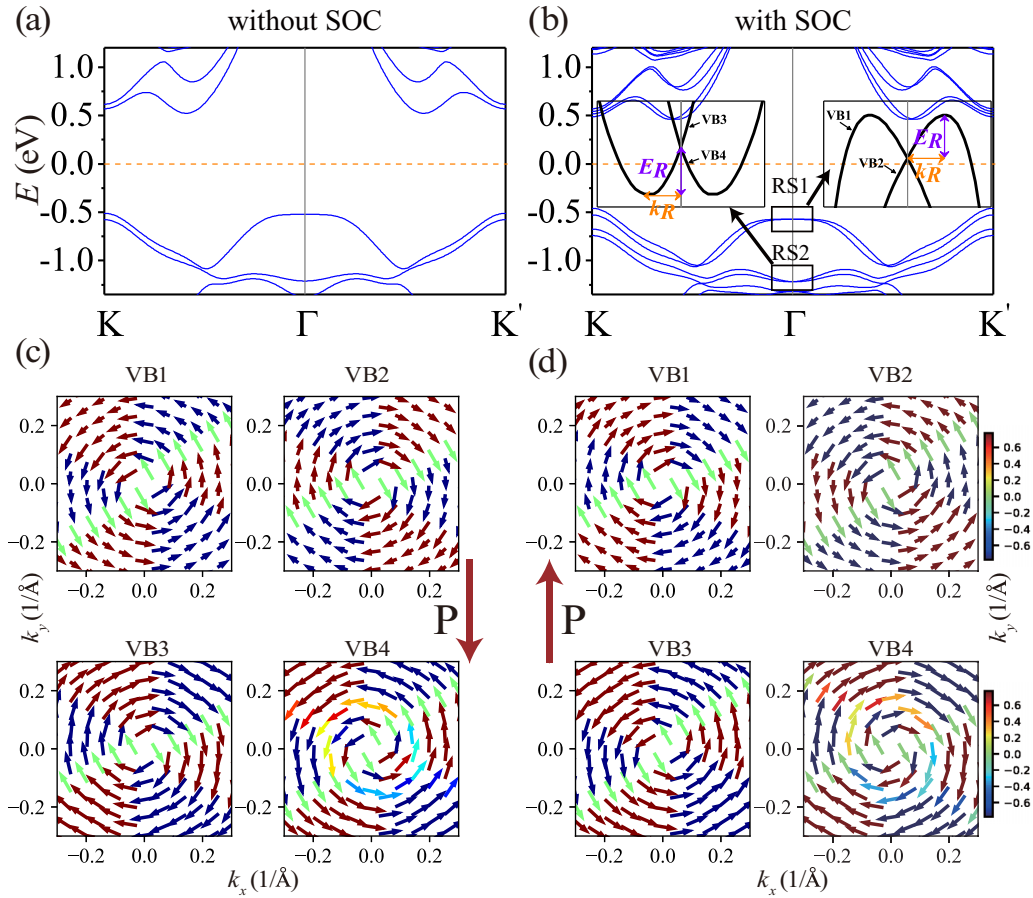
FIG. 3. Band structures of bilayer MoTe$_2$ in the AB stacking order without (a) and with (b) SOC. Insets in (b) are the enlargements of the two sets of Rashba splitting RS1 and RS2 around the Γ point. Spin textures of VB1, VB2, VB3, and VB4 for the configurations AB (c) and $A'B'$ (d) calculated by DFT. The orientations and sizes of in-plane spin components are indicated by the directions and lengths of the arrows, respectively, and the out-of-plane spin components are represented by the color scale of the arrows.

polarization, which enhances the macroscopic polarization [49,51]. However, electronic ferroelectricity, which is governed by electronic polarization instead of ionic polarization, is very rare in nature [49,52]. It is remarkable that in bilayer MX_2 studied here, the ferroelectric polarization is contributed totally by electronic polarization since there is no asymmetric distribution of ions in the z direction. Such an unusual electronic ferroelectricity promises both high-frequency and high-performance operations.

B. Rashba splitting

The out-of-plane ferroelectric polarizations in the AB and $A'B'$ structures induce Rashba splitting. Figures 3(a) and 3(b) shows the band structures of bilayer MoTe$_2$ in the AB structure without and with SOC, respectively. It is obvious that when the SOC is included, the spin degeneracy is lifted, introducing two sets of Rashba splitting (denoted as RS1 and RS2) around the Γ point in the first highest two valence bands (named VB1 and VB2) and the second highest two valence bands (named VB3 and VB4), respectively. The $A'B'$ structure that is energetically degenerate with AB shows the same electronic structures and Rashba band dispersions as AB. By contrast, in

other nonferroelectric structures, no Rashba splitting is found around Γ.

The strength of the Rashba effect can be characterized by the Rashba coefficient λ that is approximated as $\lambda = 2E_R/k_R$, where E_R and k_R are the energy difference and the momentum offset between the band degeneracy point (Γ) and the band extremum, respectively [see the insets of Fig. 3(b)]. For bilayer MoTe$_2$ in the ferroelectric AB or $A'B'$ structure, we obtain Rashba coefficients of 0.026 and 0.058 eV Å for the two sets of Rashba splitting RS1 and RS2, respectively, comparable to the values in the InGaAs/InAlAs interface and the Pb thin film [53,54]. We also list the λ for other bilayer MX_2 in Table II.

We further calculate the expectation values of the spin operators $\langle S_i(k) \rangle = \langle \psi(k)|\sigma_i|\psi(k) \rangle$, where $\psi(k)$ is the spinor wave function, σ_i is the Pauli spin matrix, and $i = x, y, z$. The obtained spin textures for the Rashba bands of bilayer MoTe$_2$ in the AB and $A'B'$ structures are shown in Figs. 3(c) and 3(d). For each set of Rashba splitting, we can clearly observe typical Rashba spin patterns where the in-plane spin components of the upper and lower bands involved in the Rashba splitting rotate in opposite directions (one direction is clockwise while the other is counterclockwise). We note that
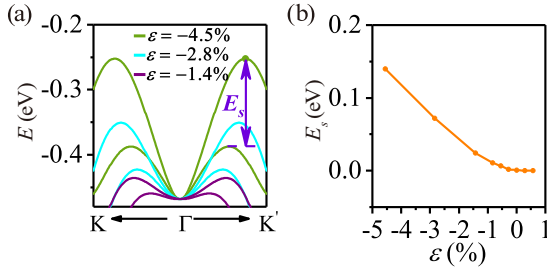
FIG. 4. (a) Evolutions of the RS1 bands with increasing in-plane compressive strain. Violet, cyan, and green curves are for the strains of -1.4%, -2.8%, and -4.5%, respectively. (b) Magnitudes of Rashba band splitting E_S under different strains.

the two sets of Rashba splitting in the AB (or $A'B'$) structure of bilayer MoTe$_2$ have exactly opposite spin textures. Taking AB as an example, the upper and lower bands (VB1 and VB2) for the RS1 have counterclockwise and clockwise spin textures, respectively, while the upper and lower bands (VB3 and VB4) for the RS2 have clockwise and counterclockwise spin textures, respectively.

One remarkable characteristic for FRSCs is that their spin textures can be manipulated by switching their ferroelectric polarizations. From the AB to the $A'B'$ structure, as the polarization direction changes from $-z$ to $+z$, the in-plane spin textures of the two sets of Rashba bands are both reversed [see Figs. 3(c) and 3(d)]. This offers an electronic and nonvolatile way to control spin in these bilayer TMD materials. However, unlike the in-plane spin texture, the out-of-plane spin polarizations remain unchanged upon the inversion of the out-of-plane ferroelectric polarization. This can be understood as follows. Considering spin-orbit coupling, electrons in motion experience an effective magnetic field $\boldsymbol{B} = (\boldsymbol{p} \times \boldsymbol{E}/2mc^2)$ [55–57]. The out-of-plane spin polarizations mainly arise from in-plane dipole moments, which are the same in the AB and $A'B'$ structures, and consequently the two structures have nearly equal out-of-plane spin polarizations.

We find that the Rashba energy splitting can be effectively tuned by applying an in-plane biaxial strain. Because the RS1 is located in the highest valence bands and more easily utilized in the practical devices, we focus on the strain effects on the RS1. Figure 4(a) shows the evolutions of the VB1 and VB2 involved in the RS1 with different compressive biaxial strains. As the electronic states of VB1 and VB2 near the Γ point mainly consist of the Mo d_{z^2} orbitals pointing to the out-of-plane direction but those away from the Γ point are dominated by the in-plane Mo d_{xy}, $d_{x^2-y^2}$ orbitals, the electronic states away from Γ are more sensitive to the applied biaxial strain than those near Γ [58]. Therefore, the shape of VB1 and VB2 (VB2 in particular) will be largely changed by the biaxial strain, as shown in Fig. 4(a). In this case, λ is no longer a well-defined physical quantity. However, the Rashba energy splitting E_S can still be well defined as the energy difference between the maxima of the VB1 and VB2. At small strains where the maximum of VB2 is located at the band degeneracy point Γ, E_S is equal to E_R mentioned above. With increasing compressive biaxial strain, it is remarkable that E_S is rapidly raised [see Fig. 4(b)]. When the compressive

strain reaches about 4%, E_S even exceeds 100 meV, larger than the value reported for BiTeI [20] where a giant Rashba effect was invoked. Additionally, it is worth mentioning that compressive biaxial strain can be introduced in 2D materials by two typical methods. In the first method, the 2D material is put on a piezoelectric substrate, and the substrate can be controllably shrunk in the horizontal direction by applying an electric field, subjecting the 2D material to a uniform compressive biaxial strain [59]. The second method is utilizing the thermal expansion mismatch between the 2D material and the underlying substrate. By intentionally selecting a substrate that has a smaller thermal expansion coefficient than the 2D material, a biaxial compressive strain could be introduced into the supported 2D material when the substrate is heated [60,61].

C. $\boldsymbol{k} \cdot \boldsymbol{p}$ model for the Rashba splitting in bilayer TMD

We develop a $\boldsymbol{k} \cdot \boldsymbol{p}$ model based on the symmetry analyses to understand the Rashba effects in ferroelectric bilayer MoTe$_2$. Given that the two sets of Rashba splitting emerge in four highest valence bands around the Γ point that are mainly composed of Mo d_{z^2} orbitals, we can ignore other orbitals and bands when we construct the $\boldsymbol{k} \cdot \boldsymbol{p}$ model. The spin degrees of freedom are described by the Pauli matrix σ_i ($i = 0, x, y, z$), and the freedom of the layer pseudospin degree is also included by using another Pauli matrix τ_i ($i = 0, x, y, z$). The effective low-energy Hamiltonian can be deduced by identifying all symmetry-allowed terms, which yields (more details can be found in the Appendix)

$$
\begin{aligned}
H(k) &= H_m(k) + H_R(k) + H_I(k), \\
H_m(k) &= \frac{k^2}{2m^*}\tau_0\sigma_0 + \beta(k)\tau_0\sigma_z + \alpha_m\tau_z(-k_y\sigma_x + k_x\sigma_y), \\
H_R(k) &= \alpha_R(k)\tau_0(-k_y\sigma_x + k_x\sigma_y) + \alpha_e(k)\tau_z\sigma_0, \\
H_I(k) &= \alpha_I\tau_x\sigma_0,
\end{aligned}
\tag{1}
$$

where $\beta(k) = \beta(k_x^2 - 3k_y^2)k_x$, $\alpha_R(k) = \alpha_R(1 + \gamma_0 k^2)$, and $\alpha_e(k) = \alpha_e(1 + \gamma_1 k^2)$. The bases are $|t, \uparrow\rangle$, $|t, \downarrow\rangle$, $|b, \uparrow\rangle$, and $|b, \downarrow\rangle$, where the indices t and b refer to the top and the bottom layers, respectively. $\uparrow$ ($\downarrow$) denotes a spin-up (-down) state. In this Hamiltonian $H(k)$, the $\frac{k^2}{2m^*}$ term is a trivial energy dispersion term, the $\beta(k)$ term corresponds to out-of-plane spin polarization, the $\alpha_e(k)$ term originates from the net spontaneous polarization, which results in an energy difference between the top and bottom layers, and the $\alpha_R(k)$ and α_m terms are Rashba-type Hamiltonian terms, thus accounting for the Rashba splitting found in ferroelectric bilayer MoTe$_2$. It is noted that these two Rashba-type Hamiltonian terms are due to C_{3v} symmetry. All terms in $H_m(k)$ keep m_z symmetry but break inversion symmetry, while all terms in $H_R(k)$ break both m_z and inversion symmetries, because of the spontaneous polarization along the z direction. The term $H_I(k)$ describes the spin-independent interlayer interaction. Only the zero-order interlayer term in k is included in $H_I(k)$ since the higher-order interlayer interaction is relatively weak.

Figure 5 displays the band structures obtained by $H(k)$ in three-dimensional k space, which shows two sets of Rashba splitting with characteristic spin-momentum-locked spin textures, in good agreement with our first-principles calculation
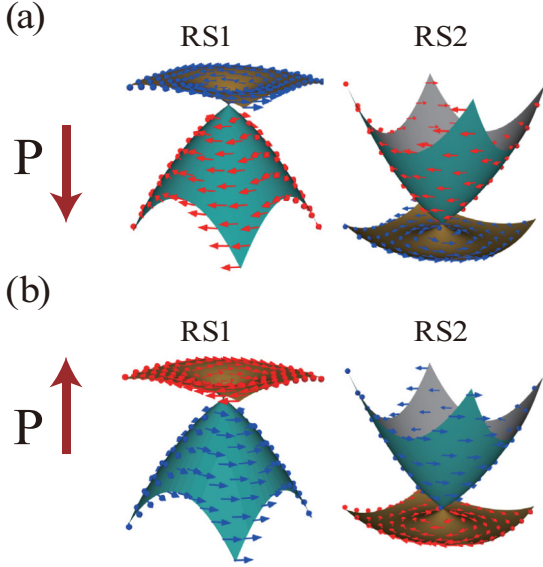
FIG. 5. Bulk band structures with corresponding spin textures derived from the $\boldsymbol{k} \cdot \boldsymbol{p}$ model when the polarization is along the $-z$ (a) and $+z$ (b) direction. Red and blue arrows represent anticlockwise and clockwise rotation orientations, respectively.

results. Concretely speaking, according to Eq. (A4), the in-plane rotation orientations of the spin textures in the two sets of Rashba splitting are determined by the signs of $\alpha_R(k) + \alpha_m$ and $\alpha_R(k) - \alpha_m$, respectively. The rotation orientations of the spin textures of the two sets of Rashba splitting are the same if the amplitude of α_m is smaller than that of $\alpha_R(k)$, and opposite otherwise, as found in the bilayer MoTe$_2$. When the ferroelectric polarization is switched, both the $\alpha_R(k)$ and α_m change signs, resulting in simultaneous reversals of in-plane rotation orientations of spin textures of the two groups of Rashba splitting.

Furthermore, it is noted that the Rashba terms $\alpha_m(k)$ and $\alpha(k)$ originate from the intralayer SOC, so they are sensitive to the in-plane strain, which directly induces variations of the intralayer bond lengths. Under in-plane biaxial compressive strain, the M-X bond length in each layer is shortened, leading to the increase of the intralayer electronic hopping and SOC, and consequently Rashba band splitting will be enhanced, as found by our first-principles calculations shown in Fig. 4(b). By contrast, the in-plane biaxial tensile strain will weaken the intralayer SOC and thus the Rashba splitting. According to our $\boldsymbol{k} \cdot \boldsymbol{p}$ model, one can expect that ferroelectricity tunable Rashba splitting always occurs when two atomic layers with C_{3v} symmetry are stacked asymmetrically, and strengthening intralayer SOC is a promising way to enhance Rashba band splitting.

IV. CONCLUSION

In summary, using first-principles calculations combined with a $\boldsymbol{k} \cdot \boldsymbol{p}$ model analysis, we predict that bilayer 2H-MX_2 are novel 2D FRSCs in which electronic ferroelectricity and Rashba splitting coexist and couple to each other. When two

single-layer MX_2 are stacked in AB or AB' order, which breaks both the inversion and mirror symmetry, a net interface dipole is formed, introducing a spontaneous out-of-plane ferroelectric polarization. The ferroelectricity further results in the emergence of the Rashba spin splitting with the corresponding spin textures in the (k_x, k_y) plane switchable via changing the direction of the ferroelectric polarization. More interestingly, the Rashba band splitting strength can be tuned to be comparable to that of the giant Rashba semiconductor BiTeI by applying a small in-plane compressive strain. These findings can not only open avenues for interplay between ferroelectricity and the Rashba effect in the 2D limit, but they also may lead to designing a new generation of spintronic devices with electrically controllable spin.

APPENDIX: DERIVATION OF THE $\boldsymbol{k} \cdot \boldsymbol{p}$ MODEL

The $\boldsymbol{k} \cdot \boldsymbol{p}$ Hamiltonian is derived according to the theory of invariants [62,63]. This method relies on the fact that the Hamiltonian must satisfy all symmetric operators of the system regardless of microscopic details. If we consider a system characterized by a point group G, we can write down its matrix representation $\{D(g) : g \in G\}$ once the basis function is obtained. The derived Hamiltonian H should satisfy [64]

$$D(g)H(g^{-1}k)D^{-1}(g) = H(k), \quad \forall g \in G. \quad \text{(A1)}$$

Bilayer polar TMD in this work is characterized by point group C_{3v}, whose generators are C_{3z} and m_x. These two operators plus time reversal operator $\mathcal{T}$ (time reversal symmetry is always imposed in this work) should be included here to derive all symmetry-allowed terms in the $\boldsymbol{k} \cdot \boldsymbol{p}$ model in the main text. We define the symmetric operators in reciprocal space as follows:

$$\begin{aligned} C_{3z} &: (k_x, k_y, k_z) \rightarrow \left(-\tfrac{1}{2}k_x - \tfrac{\sqrt{3}}{2}k_y, \tfrac{\sqrt{3}}{2}k_x - \tfrac{1}{2}k_y, k_z \right), \\ m_x &: (k_x, k_y, k_z) \rightarrow (-k_x, k_y, k_z), \\ \mathcal{T} &: (k_x, k_y, k_z) \rightarrow (-k_x, -k_y, -k_z). \end{aligned} \quad \text{(A2)}$$

With the basis function we use in the main text we can get the matrix forms of symmetric operators in the spin and layer pseudospin spaces. In the spin space, we can write down the matrix forms of symmetry operators. The time-reversal symmetry $\mathcal{T}$ is expressed as $\mathcal{T} = i\sigma_y \mathcal{K}$, and $\mathcal{K}$ is complex conjugation. The C_{3z} operator is $\exp(-i\pi\hat{\sigma}_z/3)$ and the m_x operator is $-i\sigma_x$. Similarly, in the layer pseudospin space we write $\mathcal{T} = \tau_0$, $C_{3z} = \tau_0$, and $m_x = \tau_x$.

After writing down all three of these symmetric operators, we can check all possible allowed terms constrained in the (k_x, k_y) plane. Without considering interlayer interaction, all

terms that are invariant under the transformation of the symmetric operators up to the cubic order in $\boldsymbol{k}$ form $H_m(k)$ and $H_R(k)$. For interlayer interaction, we only consider the zeroth-order interlayer term in k since the higher-order interlayer interaction is relatively weak, which results in $H_I(k)$ in the main text. Finally, the Hamiltonian arrives at

$$H(k) = H_m(k) + H_R(k) + H_I(k),$$

$$H_m(k) = \frac{k^2}{2m^*}\tau_0\sigma_0 + \beta(k)\tau_0\sigma_z + \alpha_m\tau_z(-k_y\sigma_x + k_x\sigma_y),$$

$$H_R(k) = \alpha_R(k)\tau_0(-k_y\sigma_x + k_x\sigma_y) + \alpha_e(k)\tau_z\sigma_0,$$

$$H_I(k) = \alpha_I\tau_x\sigma_0,$$

(A3)

and the matrix form of the Hamiltonian is

$$
\begin{pmatrix}
\frac{k^2}{2m^*} + \beta(k) + \alpha_e(k) & [\alpha_R(k) + \alpha_m](-k_y - ik_x) & \alpha_I & 0 \\
[\alpha_R(k) + \alpha_m](-k_y + ik_x) & \frac{k^2}{2m^*} - \beta(k) + \alpha_e(k) & 0 & \alpha_I \\
\alpha_I & 0 & \frac{k^2}{2m^*} + \beta(k) - \alpha_e(k) & [\alpha_R(k) - \alpha_m](-k_y - ik_x) \\
0 & \alpha_I & [\alpha_R(k) - \alpha_m](-k_y + ik_x) & \frac{k^2}{2m^*} - \beta(k) - \alpha_e(k)
\end{pmatrix}.
$$

(A4)

In this Hamiltonian $H(k)$, $\frac{k^2}{2m^*}$ describes the trivial energy dispersion term. The $\alpha_e(k)$ term determines the energy difference between the top and bottom layers due to the net spontaneous polarization. The $\beta(k)$ term corresponds to out-of-plane spin polarization. The $\alpha_R(k)$ and α_m terms are Rashba-type Hamiltonian terms, thus accounting for the Rashba splitting found in ferroelectric bilayer MoTe$_2$. The term $H_I(k)$ describes the spin-independent interlayer interaction.

[1] S. Picozzi, Front. Phys. **2**, 10 (2014).

[2] J. Varignon, J. Santamaria, and M. Bibes, Phys. Rev. Lett. **122**, 116401 (2019).

[3] I. Žutić, J. Fabian, and S. D. Sarma, Rev. Mod. Phys. **76**, 323 (2004).

[4] D. D. Sante, P. Barone, R. Bertacco, and S. Picozzi, Adv. Mater. **25**, 509 (2013).

[5] C. Rinaldi, S. Varotto, M. Asa, J. Sławińska, J. Fujii, G. Vinai, S. Cecchi, D. D. Sante, R. Calarco, I. Vobornik et al., Nano Lett. **18**, 2751 (2018).

[6] M. Liebmann, C. Rinaldi, D. Di Sante, J. Kellner, C. Pauly, R. N. Wang, J. E. Boschker, A. Giussani, S. Bertoli, M. Cantoni et al., Adv. Mater. **28**, 560 (2016).

[7] L. G. D. da Silveira, P. Barone, and S. Picozzi, Phys. Rev. B **93**, 245159 (2016).

[8] A. Narayan, Phys. Rev. B **92**, 220101(R) (2015).

[9] H. Djani, A. C. Garcia-Castro, W.-Y. Tong, P. Barone, E. Bousquet, S. Picozzi, and P. Ghosez, arXiv:1903.01241.

[10] M. Coll, A. Gomez, E. Mas-Marza, O. Almora, G. Garcia-Belmonte, M. Campoy-Quiles, and J. Bisquert, J. Phys. Chem. Lett. **6**, 1408 (2015).

[11] N. Setter, D. Damjanovic, L. Eng, G. Fox, S. Gevorgian, S. Hong, A. Kingon, H. Kohlstedt, N. Y. Park, G. B. Stephenson et al., J. Appl. Phys. (Melville, NY) **100**, 051606 (2006).

[12] J. F. Scott, Science **315**, 954 (2007).

[13] T. Birol, Nature (London) **560**, 174 (2018).

[14] F. Liu, L. You, K. L. Seyler, X. Li, P. Yu, J. Lin, X. Wang, J. Zhou, H. Wang, H. He et al., Nat. Commun. **7**, 12357 (2016).

[15] W. Ding, J. Zhu, Z. Wang, Y. Gao, D. Xiao, Y. Gu, Z. Zhang, and W. Zhu, Nat. Commun. **8**, 14956 (2017).

[16] J. Xiao, H. Zhu, Y. Wang, W. Feng, Y. Hu, A. Dasgupta, Y. Han, Y. Wang, D. A. Muller, L. W. Martin et al., Phys. Rev. Lett. **120**, 227601 (2018).

[17] F. Xue, W. Hu, K.-C. Lee, L.-S. Lu, J. Zhang, H.-L. Tang, A. Han, W.-T. Hsu, S. Tu, W.-H. Chang et al., Adv. Funct. Mater. **28**, 1803738 (2018).

[18] C. R. Ast, J. Henk, A. Ernst, L. Moreschini, M. C. Falub, D. Pacilé, P. Bruno, K. Kern, and M. Grioni, Phys. Rev. Lett. **98**, 186807 (2007).

[19] I. Gierz, T. Suzuki, E. Frantzeskakis, S. Pons, S. Ostanin, A. Ernst, J. Henk, M. Grioni, K. Kern, and C. R. Ast, Phys. Rev. Lett. **103**, 046803 (2009).

[20] K. Ishizaka, M. S. Bahramy, H. Murakawa, M. Sakano, T. Shimojima, T. Sonobe, K. Koizumi, S. Shin, H. Miyahara, A. Kimura et al., Nat. Mater. **10**, 521 (2011).

[21] Z. Zhong, L. Si, Q. Zhang, W.-G. Yin, S. Yunoki, and K. Held, Adv. Mater. Int. **2**, 1400445 (2015).

[22] V. V. Volobuev, P. S. Mandal, M. Galicka, O. Caha, J. Sánchez-Barriga, D. Di Sante, A. Varykhalov, A. Khiar, S. Picozzi, G. Bauer et al., Adv. Mater. **29**, 1604185 (2017).

[23] M. Wu and X. C. Zeng, Nano Lett. **16**, 3236 (2016).

[24] L. Li and M. Wu, ACS Nano **11**, 6382 (2017).

[25] S. N. Shirodkar and U. V. Waghmare, Phys. Rev. Lett. **112**, 157601 (2014).

[26] D. Di Sante, A. Stroppa, P. Barone, M.-H. Whangbo, and S. Picozzi, Phys. Rev. B **91**, 161401(R) (2015).

[27] G. Kresse and J. Hafner, Phys. Rev. B **47**, 558 (1993).

[28] G. Kresse and J. Furthmüller, Comput. Mater. Sci. **6**, 15 (1996).

[29] G. Kresse and D. Joubert, Phys. Rev. B **59**, 1758 (1999).

[30] J. P. Perdew, K. Burke, and M. Ernzerhof, Phys. Rev. Lett. **77**, 3865 (1996).

[31] J. P. Perdew, K. Burke, and M. Ernzerhof, Phys. Rev. Lett. **78**, 1396 (1997).

[32] S. Grimme, J. Antony, S. Ehrlich, and H. Krieg, J. Phys. Chem. Lett. **132**, 154104 (2010).

[33] G. Henkelman, B. P. Uberuaga, and H. Jonsson, J. Chem. Phys. **113**, 9901 (2000).

[34] R. D. King-Smith and D. Vanderbilt, Phys. Rev. B **47**, 1651(R) (1993).

[35] J. He, K. Hummer, and C. Franchini, Phys. Rev. B **89**, 075409 (2014).

[36] G. Constantinescu, A. Kuc, and T. Heine, Phys. Rev. Lett. **111**, 036104 (2013).

[37] T. Cusati, A. Fortunelli, G. Fiori, and G. Iannaccone, Phys. Rev. B **98**, 115403 (2018).

[38] J. A. Wilson and A. Yoffe, Adv. Phys. **18**, 193 (1969).

[39] L. C. Towle, V. Oberbeck, B. E. Brown, and R. E. Stajdohar, Science **154**, 895 (1966).

[40] S. M. Shinde, K. P. Dhakal, X. Chen, W. S. Yun, J. Lee, H. Kim, and J.-H. Ahn, NPG Asia Mater. **10**, e468 (2018).

[41] J. Yan, J. Xia, X. Wang, L. Liu, J.-L. Kuo, B. K. Tay, S. Chen, W. Zhou, Z. Liu, and Z. X. Shen, Nano Lett. **15**, 8155 (2015).

[42] J. Quereda, A. Castellanos-Gomez, N. Agraït, and G. Rubio-Bollinger, Appl. Phys. Lett. **105**, 053111 (2014).

[43] M.-L. Lin, Q.-H. Tan, J.-B. Wu, X.-S. Chen, J.-H. Wang, Y.-H. Pan, X. Zhang, X. Cong, J. Zhang, W. Ji *et al.*, ACS Nano **12**, 8770 (2018).

[44] Y. Zhang, J. Sun, J. P. Perdew, and X. Wu, Phys. Rev. B **96**, 035143 (2017).

[45] C. Si, Z. Lin, J. Zhou, and Z. Sun, 2D Mater. **4**, 015027 (2016).

[46] L. Bengtsson, Phys. Rev. B **59**, 12301 (1999).

[47] R. E. Cohen and H. Krakauer, Ferroelectrics **136**, 65 (1992).

[48] N. A. Spaldin, J. Solid State Chem. **195**, 2 (2012).

[49] K. Kobayashi, S. Horiuchi, R. Kumai, F. Kagawa, Y. Murakami, and Y. Tokura, Phys. Rev. Lett. **108**, 237601 (2012).

[50] R. Resta, Rev. Mod. Phys. **66**, 899 (1994).

[51] W. Zhong, R. D. King-Smith, and D. Vanderbilt, Phys. Rev. Lett. **72**, 3618 (1994).

[52] A. Chanana and U. V. Waghmare, Phys. Rev. Lett. **123**, 037601 (2019).

[53] J. Nitta, T. Akazaki, H. Takayanagi, and T. Enoki, Phys. Rev. Lett. **78**, 1335 (1997).

[54] J. H. Dil, F. Meier, J. Lobo-Checa, L. Patthey, G. Bihlmayer, and J. Osterwalder, Phys. Rev. Lett. **101**, 266802 (2008).

[55] G. Dresselhaus, Phys. Rev. **100**, 580 (1955).

[56] Y. A. Bychkov and E. I. Rashba, JETP Lett. **39**, 78 (1984).

[57] H. Yuan, M. S. Bahramy, K. Morimoto, S. Wu, K. Nomura, B.-J. Yang, H. Shimotani, R. Suzuki, M. Toh, C. Kloc *et al.*, Nat. Phys. **9**, 563 (2013).

[58] Z. Y. Zhu, Y. C. Cheng, and U. Schwingenschlögl, Phys. Rev. B **84**, 153402 (2011).

[59] Y. Y. Hui, X. Liu, W. Jie, N. Y. Chan, J. Hao, Y.-T. Hsu, L.-J. Li, W. Guo, and S. P. Lau, ACS Nano **7**, 7126 (2013).

[60] C. Si, Z. Sun, and F. Liu, Nanoscale **8**, 3207 (2016).

[61] R. Roldán, A. Castellanos-Gomez, E. Cappelluti, and F. Guinea, J. Phys.: Condens. Matter **27**, 313201 (2015).

[62] G. L. Bir and G. E. Pikus, *Symmetry and Strain-induced Effects in Semiconductors* (Wiley, New York, 1974).

[63] J. Luttinger, Phys. Rev. **102**, 1030 (1956).

[64] R. Winkler, S. Papadakis, E. De Poortere, and M. Shayegan, *Spin-Orbit Coupling in Two-Dimensional Electron and Hole Systems* (Springer, Berlin, 2003).